JACS
JOURNAL OF THE AMERICAN CHEMICAL SOCIETY
Article
pubs.acs.org/JACS

Complex Columnar Hexagonal Polymorphism in Supramolecular Assemblies of a Semifluorinated Electron-Accepting Naphthalene Bisimide

Yu-Chun Wu,[†] Pawaret Leowanawat,[†] Hao-Jan Sun,[†,‡] Benjamin E. Partridge,[†] Mihai Peterca,[†] Robert Graf,[§] Hans W. Spiess,[§] Xiangbing Zeng,[∥] Goran Ungar,[∥,#] Chain-Shu Hsu,[⊥] Paul A. Heiney,[‡] and Virgil Percec*[,†]

[†]Roy and Diana Vagelos Laboratories, Department of Chemistry, University of Pennsylvania, Philadelphia, Pennsylvania 19104-6323, United States

[‡]Department of Physics and Astronomy, University of Pennsylvania, Philadelphia, Pennsylvania 19104-6396, United States

[§]Max-Planck Institute for Polymer Research, 55128 Mainz, Germany

[∥]Department of Materials Science and Engineering, University of Sheffield, Sheffield S1 3JD, United Kingdom

[#]Department of Physics, Zhejiang Sci-Tech University, Hangzhou 310018, China

[⊥]Department of Applied Chemistry, National Chiao Tung University, Hsin-Chu 30049, Taiwan

Supporting Information

ABSTRACT: Simple synthetic methods for a strongly electron-accepting naphthalene bisimide (NBI) derivative functionalized with a new environmentally friendly chiral racemic semifluorinated alkyl group and with AB_3 minidendrons containing the same semifluorinated group are reported. The semifluorinated dendron was attached to the imide groups of the NBI via one, two, and three (m = 1, 2, 3) methylenic units. The NBI-containing semifluorinated groups and the dendronized NBI with m = 1 and 2 self-organize into lamellar crystals. The dendronized NBI with m = 3 self-assembles into an unprecedentedly complex and ordered column that self-organizes in a columnar hexagonal periodic array. This array undergoes a continuous transition to a columnar hexagonal superlattice that does not display a first-order phase transition during analysis by differential scanning calorimetry at heating and cooling rates of 10 and 1 °C/min. These complex columnar hexagonal periodic arrays with intramolecular order could be elucidated only by a combination of powder and fiber X-ray diffraction studies and solid-state NMR experiments. The lamellar crystals self-organized from m = 1 and the two highly ordered columnar hexagonal periodic arrays of m = 3 are assembled via thermodynamically controlled processes. Since strongly electron-accepting derivatives are of great interest to replace fullerene acceptors in organic photovoltaics and for other supramolecular electronic materials, the multitechnique structural analysis methodology elaborated here must be taken into consideration in all related studies.

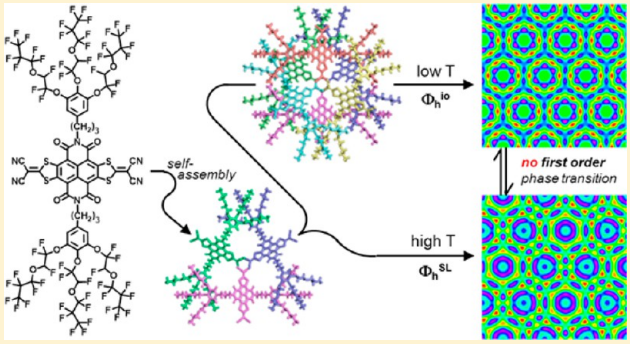

INTRODUCTION

Perylene bisimide (PBI)[1−3] and naphthalene bisimide (NBI)[4] derivatives are versatile electron-accepting building blocks employed in a diversity of supramolecular and macromolecular architectures, with functions ranging from artificial photosynthetic systems[5,6] and mimics of biological membranes[7] to n-type semiconductors and field-effect transistors,[8,9a] as replacements to fullerene acceptors in organic photovoltaics[9b−d] and models to elucidate supramolecular polymerization in solvophobic organic solvents and in water,[10−12] among many others. There are only limited examples in which the packing of PBI and NBI molecules is understood at the molecular level of supramolecular assemblies. In these examples the complex arrangements of simple PBIs and NBIs have been accessed mostly by single crystal investigations.[13] However, larger PBI and NBI derivatives form kinetically controlled 2D and 3D polymorphic assemblies, and therefore even the identification of ordered polymorphs is often extremely difficult.[14−16]

Our laboratory discovered that for a series of PBI derivatives dendronized with two first generation self-assembling minidendrons, (3,4,5)nG1-m-PBI (where n is the number of carbons in the alkyl groups and m is the number of methylenic units between the dendron and the imide group of PBI), a careful selection of n and m can transform crystallization of the supramolecular assembly from a kinetically controlled process

Received: October 16, 2014
Published: December 30, 2014

DOI: 10.1021/ja510643b
J. Am. Chem. Soc. 2015, 137, 807−819

Scheme 1. Synthesis of Semifluorinated Linear and Minidendritic Precursors with m = 1, 2, 3[a]

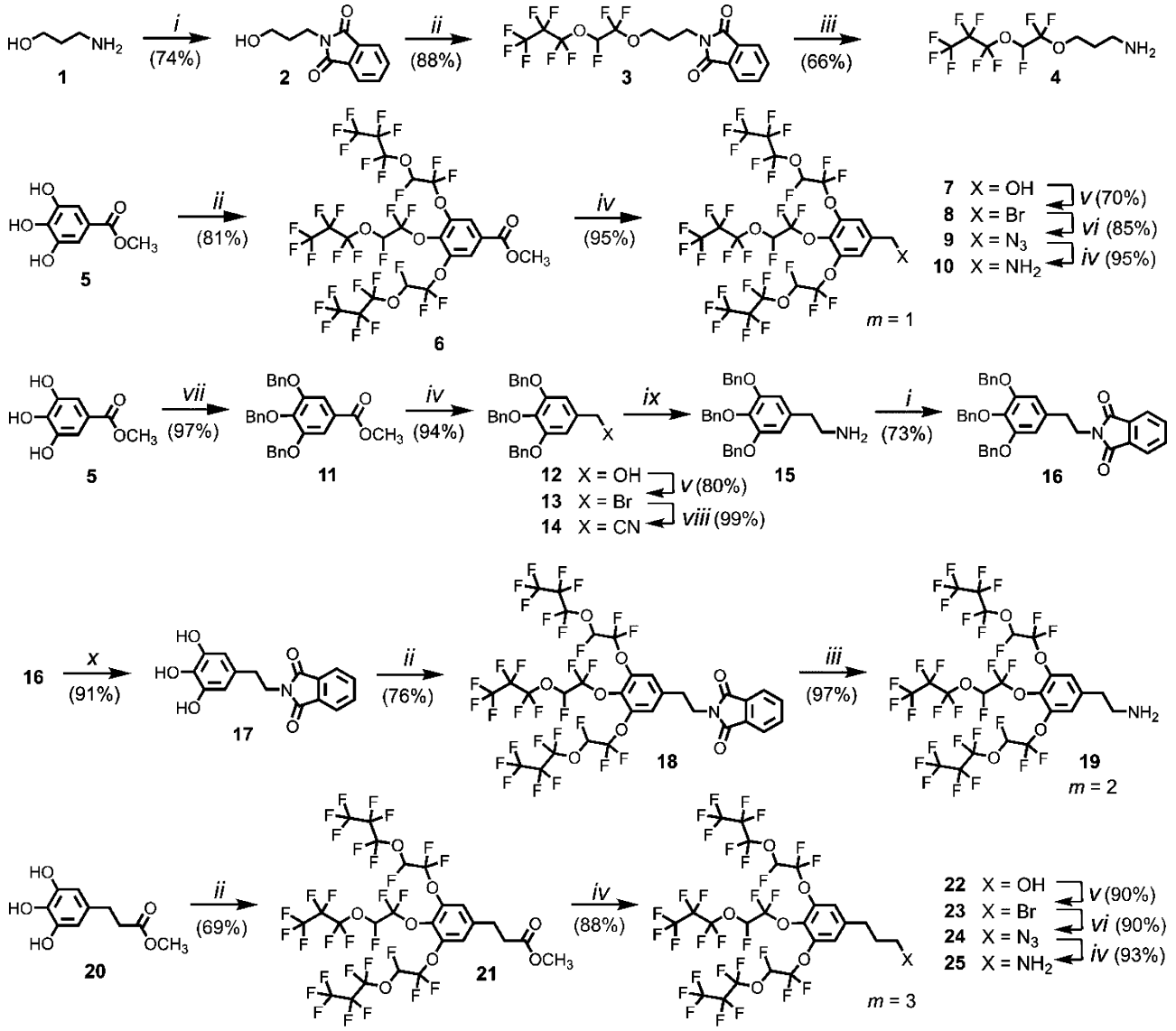

[a]Reagents and conditions: (i) Phthalic anhydride, DMAP (120 °C); (ii) ^{t}BuOK, CF_2=$CFOC_3F_7$, DMF; (iii) NH_2-NH_2.H_2O, EtOH-THF (reflux); (iv) $LiAlH_4$, THF (0 °C); (v) CBr_4, PPh_3, THF (0 °C); (vi) NaN_3, DMF; (vii) BnCl, K_2CO_3, CH_3CN (80 °C); (viii) NaCN, benzyltriethylammonium chloride, DMF; (ix) 1 M BH_3-THF, THF (reflux); (x) H_2, Pd/C, THF-EtOH (25 °C).

into a thermodynamically controlled process.[14] This discovery facilitates fast access to equilibrium states, to their functions, and to the determination of their structures regardless of the thermal history of the sample.[14]

Here we report the simple synthesis of a new series of strongly electron-accepting NBI derivatives,[17] with m = 1, 2, or 3, functionalized with twin-semifluorinated and environmentally friendly chiral racemic dendrons elaborated recently in our laboratory.[18] These compounds represent, most probably, some of the most strongly electron-accepting self-organizable molecules. Fluorinated fragments are commonly introduced in supramolecular electronics to protect them from moisture.[19−28] Previous studies had found that linear semifluorinated alkyl groups induced the self-assembly of dendrons of the first generation, compared to the second or third generations required for hydrogenated analogs, while simultaneously providing protection against moisture.[19−28] However, the ideal structures of semifluorinated first generation dendrons investigated so far contain fragments that degrade to form the toxic and biopersistent perfluorooctanoic acid and higher homologues that are prohibited by the Environmental Protection Agency.[18,29−32] In contrast, the most recent semifluorinated dendrons elaborated in our laboratory[18] degrade to give environmentally acceptable gallic acid and perfluoropropyl chains that are, respectively, nontoxic and not biopersistent.[33,34] Furthermore, the presence of an oxygen ether bond and a chiral racemic and acidic proton in the peripheral fluorinated chain enhances the solubility of the dendronized NBIs in organic solvents.

In this report semifluorinated chains with a number of carbon atoms within the range of values that are expected to result in thermodynamically controlled self-organization, as determined previously with PBIs dendronized with hydrogenated minidendrons, were synthesized and incorporated to the imide groups of a strongly electron-accepting NBI.[14,35,36] NBI with m = 1 exhibits a thermodynamically controlled

DOI: 10.1021/ja510643b
J. Am. Chem. Soc. 2015, 137, 807−819

Scheme 2. Synthesis of the Semifluorinated Linear and Dendronized NBI Derivatives 34, 35, 36, and 37[a]

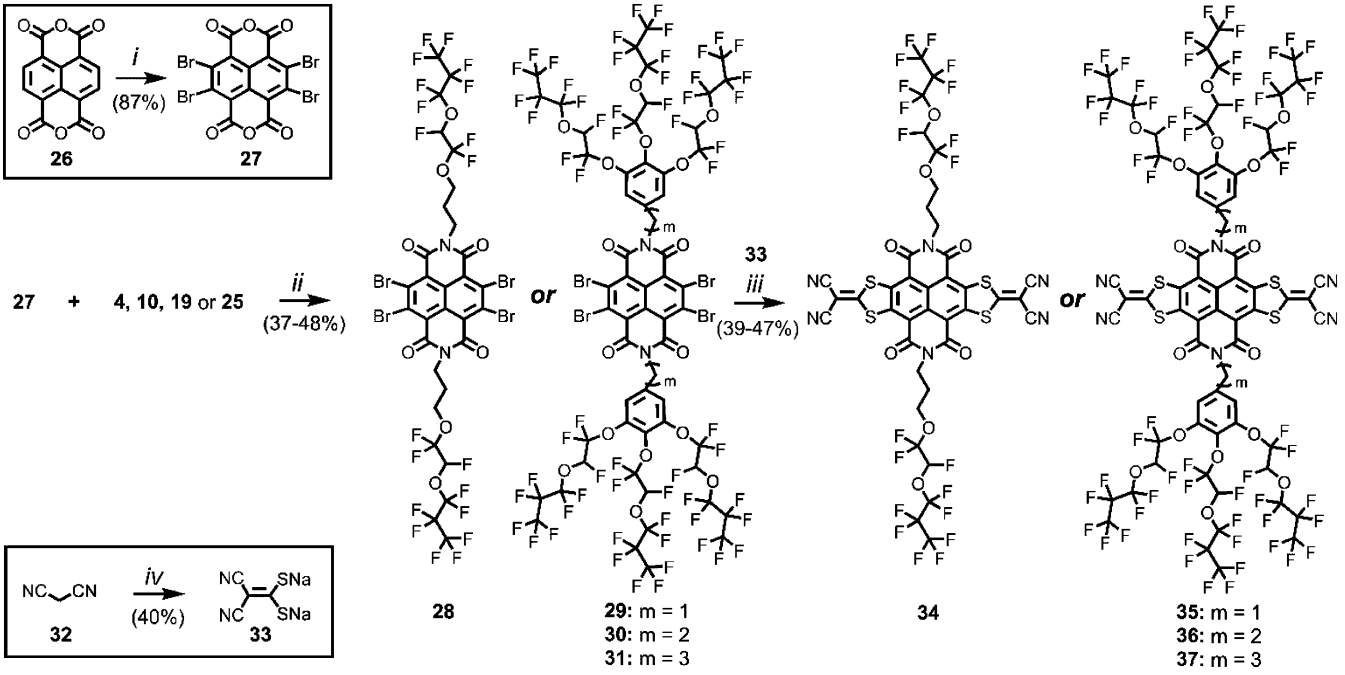

[a]Reagents and conditions: (i) Dibromoisocyanuric acid, oleum, 3 h (RT); (ii) CH_3COOH, DMF-toluene, 30 min (100 °C) then PBr_3, 12 h (reflux); (iii) **33**, THF, 1 h (50 °C); (iv) CS_2, NaOH, MeOH, 1 h (RT).

lamellar crystal, while a kinetically controlled lamellar crystal was displayed by the $m = 2$ compound. The derivative with $m = 3$, however, self-assembles into an unprecedentedly complex supramolecular column that self-organizes into a thermodynamically controlled columnar hexagonal lattice with intracolumnar order (Φ_h^{io}) at low temperatures and into a thermodynamically controlled superlattice at high temperatures (Φ_h^{SL}). Both structures are generated from supramolecular columns with internal order that exhibit a low degree of intercolumnar 3D correlation. Regardless of heating and cooling rates, and although both assemblies and their periodic arrays of $m = 3$ are thermodynamically controlled, no first-order phase transition could be detected by differential scanning calorimetry (DSC). Therefore, the Φ_h^{SL} superlattice could be detected and analyzed only by a combination of variable temperature (VT) X-ray diffraction (XRD) experiments and solid-state NMR studies. This unusual continuous polymorphism has, to the best of our knowledge, never been reported before in electron-acceptor-based assemblies. Given the broad range of technological applications of such assemblies, the rigorous methodology elaborated here must be given important consideration during the future structural analysis of similar supramolecular assemblies.

RESULTS AND DISCUSSION

Synthesis of Semifluorinated NBI Derivatives. The synthesis of an NBI derivative with two semifluorinated chiral racemic linear groups **34** and three NBI derivatives **35**, **36**, and **37** with two identical semifluorinated dendrons attached to the imide groups via one, two, and three methylene units ($m = 1$, 2, 3), respectively, is outlined in Schemes 1 and 2.

Protection of 3-aminopropan-1-ol **1** with phthalic anhydride in the presence of DMAP at 120 °C afforded protected amino alcohol **2** in 74% yield. Functionalization of **2** was achieved via the nucleophilic addition of **2** to perfluoropropyl vinyl ether (PPVE) in dry DMF with a catalytic amount of potassium *tert*-butoxide.[18] The resultant phthalimide **3** thus afforded in 88% yield was refluxed with hydrazine hydrate in EtOH/THF (2:1) for 3 h to give the semifluorinated linear precursor **4** in 66% yield. Two general methods were elaborated and investigated for the synthesis of the fluorinated minidendrons containing amine groups (**10**, **19**, and **25** from Scheme 1). In the first method preparation of the minidendritic precursors **10** and **25** (m = 1 and 3, respectively) proceeded first via nucleophilic addition of the corresponding 3,4,5-trihydroxy-substituted ester **5** or **20** to PPVE in dry DMF with catalytic potassium *tert*-butoxide at 0 °C to produce esters **6** and **21** in 81% and 69% yield, respectively. Conversion of the esters **6** and **21** to the corresponding amines **10** and **25** was effected via reduction with $LiAlH_4$ in dry THF at 0 °C to form the alcohols **7** and **22** (95% and 88% yield). Careful purification of alcohols **7** and **22** and of the amines **10** and **25** was required in this procedure since extended contact with strong bases can produce a small extent of side reactions. Subsequent reaction of **7** and **22** with CBr_4 and PPh_3 in dry THF at 0 °C formed bromides **8** and **23** (70% and 90% yield). Treatment of **8** and **23** with sodium azide in DMF generated azides **9** and **24** (85% and 90% yield), while their reduction with $LiAlH_4$ in dry THF gave amines **10** and **25** (95% and 93% yield, respectively).

A second approach was employed for the synthesis of $m = 2$ minidendron **19** (the phthalimide method). Benzylation of methyl gallate (**5**) with benzyl chloride in refluxing acetonitrile in the presence of K_2CO_3 gave ester **11** (97% yield), which was reduced with $LiAlH_4$ in dry THF at 0 °C to produce alcohol **12** in 94% yield. Bromination of **12** with CBr_4 and PPh_3 in dry THF at 0 °C gave bromide **13** (80% yield) which was converted quantitatively to phenylacetonitrile **14** using sodium cyanide and the phase transfer catalyst benzyltriethylammonium chloride in DMF and then reduced quantitatively to amine **15** using a borane-THF complex in dry THF. In the

DOI: 10.1021/ja510643b
J. Am. Chem. Soc. 2015, 137, 807−819

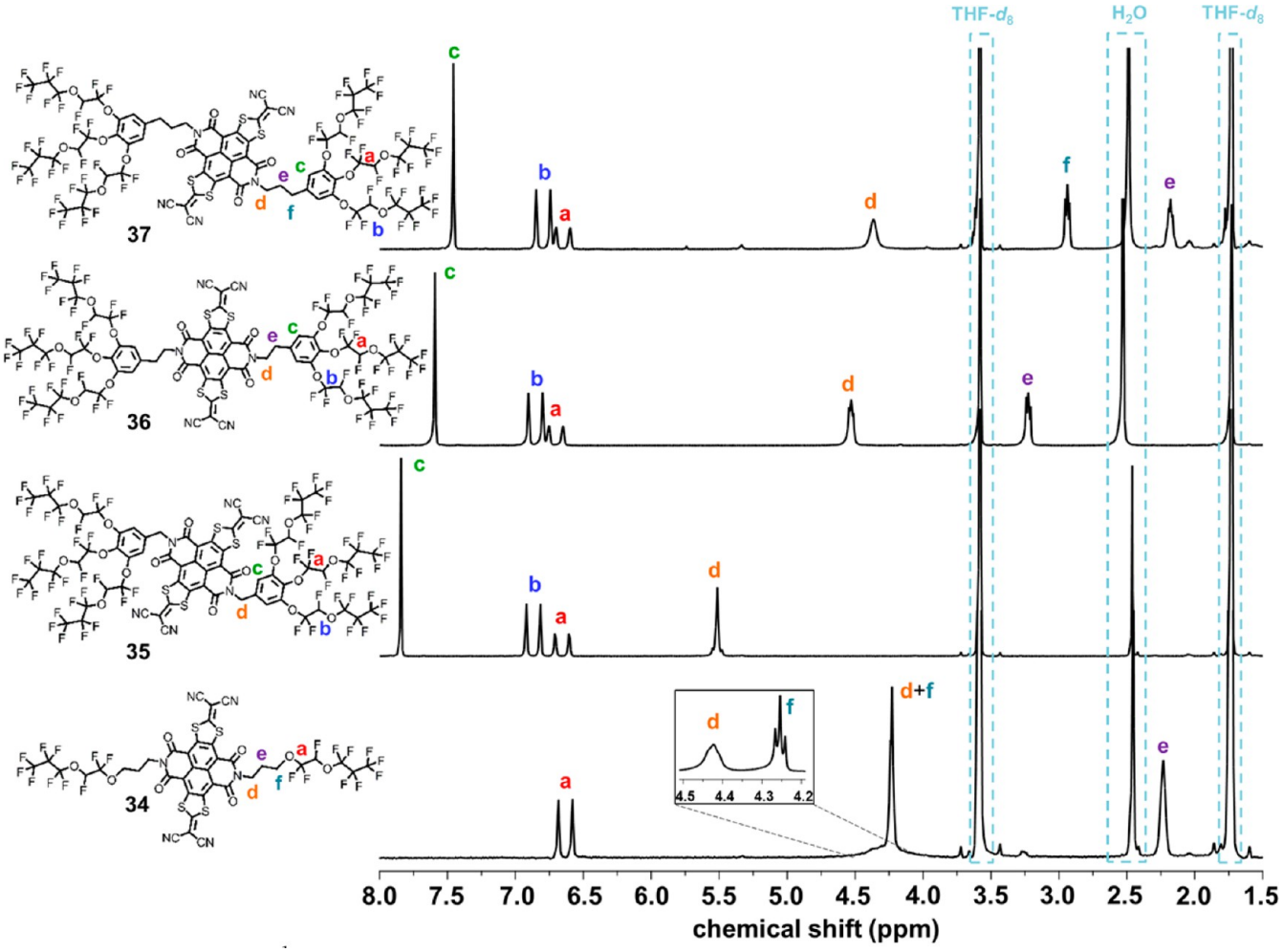

Figure 1. Excerpts of ^{1}H NMR spectra (THF-d_8, 500 MHz) of semifluorinated NBI derivatives **34**, **35**, **36**, and **37**.

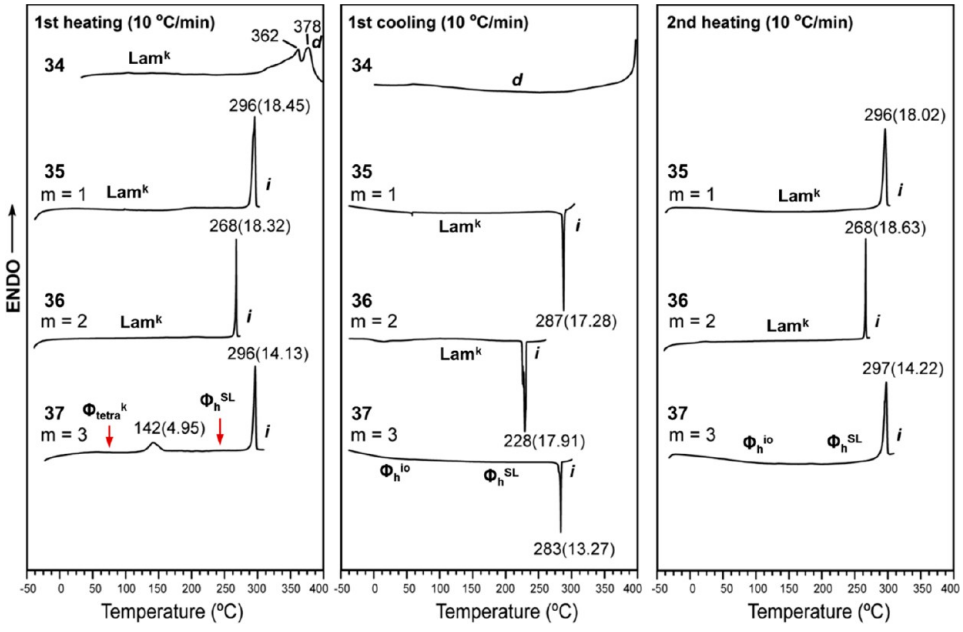

Figure 2. DSC traces of **34** and **35**, **36**, and **37** recorded with heating and cooling rates of 10 °C/min. Phases, transition temperatures, and associated enthalpy changes (in brackets in kcal/mol) are indicated. Phase notation: **Lam**^{k}, 3D lamellar crystalline phase; $\mathbf{\Phi}_{tetra}^{k}$, 3D columnar tetragonal crystalline phase; $\mathbf{\Phi}_h^{io}$, 2D hexagonal phase with intracolumnar order; $\mathbf{\Phi}_h^{SL}$, 2D hexagonal superlattice; and ***d*** denotes that the compound decomposed.

DOI: 10.1021/ja510643b
J. Am. Chem. Soc. 2015, 137, 807−819

Table 1. Transition Temperatures and Associated Enthalpy Changes of 34, 35, 36, and 37 Determined by DSC and XRD

		thermal transition (°C) and corresponding enthalpy changes (kcal/mol)	
m	rate (°C/min)	heating[a]	cooling
34	10	**Lam**^{k} 362 (−) *d*	−
35 (m = 1)	10	**Lam**^{k} 296 (15.45) *i*	*i* 287 (17.28) **Lam**^{k}
		Lam^{k} 296 (13.52) *i*	
	1	**Lam**^{k} 296 (18.16) *i*	*i* 280 (18.16) **Lam**^{k}
		Lam^{k} 298 (11.45) *i*	
36 (m = 2)	10	**Lam**^{k} 268 (18.32) *i*	*i* 228 (17.91) **Lam**^{k}
		Lam^{k} 268 (18.63) *i*	
	1	**Lam**^{k} 268 (14.90) *i*	*i* 232 (17.24) **Lam**^{k}
		Lam^{k} 268 (14.26) *i*	
37 (m = 3)	10	$\mathbf{\Phi}_{tetra}^{k}$ 142 (4.95) $\mathbf{\Phi}_{h}^{SL}$ 296 (13.13) *i*	*i* 283 (13.27) $\mathbf{\Phi}_{h}^{SL}$ − $\mathbf{\Phi}_{h}^{io}$[b]
		$\mathbf{\Phi}_{h}^{io}$ − $\mathbf{\Phi}_{h}^{SL}$[b] 297 (10.47) *i*	
	1	$\mathbf{\Phi}_{tetra}^{k}$ 132 (2.64) $\mathbf{\Phi}_{h}^{SL}$ 297 (12.48) *i*	i 286 (11.07) $\mathbf{\Phi}_{h}^{SL}$ − $\mathbf{\Phi}_{h}^{io}$[b]
		$\mathbf{\Phi}_{h}^{io}$ − $\mathbf{\Phi}_{h}^{SL}$[b] 298 (11.56) *i*	

[a]Data from the first heating and cooling scans are on the first line, and data from the second heating are on the second line, with rate indicated in second column; **Lam**^{k}, lamellar crystalline phase; $\mathbf{\Phi}_{tetra}^{k}$, columnar tetragonal crystalline phase; $\mathbf{\Phi}_{h}^{io}$, 2D simple hexagonal phase with intracolumnar order; $\mathbf{\Phi}_{h}^{SL}$, 2D hexagonal superlattice; *i*, isotropic; *d*, thermally decomposed. [b]This transition is observed by XRD. Note: quantitative uncertainties are ±1 °C for thermal transition temperatures and ∼2% for the associated enthalpy changes reported in kcal/mol.

subsequent protection reaction **15** was used without purification, to give phthalimide **16** in 73% yield after refluxing for 3 h with phthalic anhydride and a catalytic amount of DMAP. Hydrogenolysis of **16** with Pd/C in THF/EtOH (1:1) afforded *tris*-phenol **17** in 91% yield after 48 h and a subsequent recrystallization from THF/hexane. Nucleophilic addition of **17** to PPVE in dry DMF, catalyzed by potassium *tert*-butoxide, yielded dendronized phthalimide **18** (76% yield), which was refluxed with hydrazine hydrate in EtOH/THF (2:1) for 3 h to afford semifluorinated minidendron **19** in 97% yield. **19** could be used in the next step without any special purification. Both methods were used for the synthesis of **35**, **36**, and **37** and are reported in the Supporting Information. For simplicity and fewer purification steps, the second method (the phthalimide method, Scheme SS3) is recommended for all compounds reported here and for other related structures.

The tetrabromonapthalene dianhydride **27** was synthesized in 87% yield by reacting naphthalene dianhydride **26** with dibromoisocyanuric acid in oleum for 3 h.[37] Reaction of **27** with semifluorinated precursors **4**, **10**, **19**, and **25** at 100 °C with acetic acid in dry toluene/DMF (10:1) gave tetrabromonaphthalene bisimides **28**, **29**, **30**, and **31** after column chromatography (SiO_2, CH_2Cl_2, or CH_2Cl_2/hexanes (2:1)) in yields of 37−48%. Dithiolate **33** (40% yield) was synthesized from malononitrile (**32**) and CS_2 with excess NaOH in MeOH at 15 °C.[38] Subsequent condensation[39] of **33** with **28**, **29**, **30**, and **31** was achieved by stirring at 50 °C for 1 h in dry THF, to give the desired dendronized NBI derivatives **34**, **35**, **36**, and **37**, respectively, in 39−47% yield after column chromatography (SiO_2, EtOAc/CH_2Cl_2 (1:50) or EtOAc/hexanes (2:3)). Excerpts of ^{1}H NMR spectra of **34**, **35**, **36**, and **37** show clear signals pertaining to the protons of the semifluorinated chains (a, b), the aromatic protons of the aryl ether moiety of the dendron (c) and the protons of the methylene linkages (d, e, f) (Figure 1). Notable is the downfield shift (∼1 ppm) of the signal from methylene protons d in **35** compared to **36** and **37** due to enhanced deshielding by the adjacent phenyl group.

The coalescence of signals from methylene protons d and f in the spectrum of **34** may arise from the persistence of supramolecular assemblies in solution.[40] By comparison, a fully molecularly dissolved sample obtained from an incompletely dried assembly exhibits distinct signals for protons d and f (Figure 1, inset).

Identification of Supramolecular Self-Assemblies of NBI Derivatives by DSC with Different Heating and Cooling Rates and by XRD. Compounds **34**, **35**, **36**, and **37** were subjected to DSC measurements with scanning rates of 10 °C/min (Figure 2) and 1 °C/min (Figure SF1) in order to elucidate the supramolecular structures of NBI derivatives. The phase notations labeled on the DSC traces were determined by a combination of powder and fiber XRD analysis. The as prepared compound **34** self-organizes in a crystalline lamellar structure that melts above 362 °C (Figure 2, top) and starts to decompose before reaching the molten state. A comparison of Figures 2 and SF1 indicates similar DSC traces for **35** and **37** at the two different rates with only a small difference in the transition temperature and its associated enthalpy change in both heating and cooling scans. This suggests that the ordered assemblies of these compounds are thermodynamic (equilibrium) products[14−16] and that their formation is thermodynamically controlled (independent of rate). However, compound **36** (m = 2) displays a strongly supercooled phase transition (difference of 40 °C from heating to cooling traces), and therefore the formation of its supramolecular structure is kinetically controlled. For compounds **35** and **36**, with m = 1 and 2, respectively, a single lamellar crystalline phase was observed below the isotropization temperature. The crystal melting temperature of **35** is 296 °C, which is almost 30 °C higher than that of the m = 2 compound **36** (268 °C). A 9 °C supercooling was observed for the crystallization transition of **35**, while that of **36** is 40 °C. The results suggest that the short m = 1 linkage in **35** is responsible for restricted molecular mobility that leads to higher melting temperature and faster self-assembly kinetics. Compared with dendronized perylene bisimides (PBIs) from previous studies where various 2D and 3D columnar phases were observed for n = 6 to 12 and m = 0 to 4,[14] no columnar assembly and no columnar periodic array were identified in the fluorinated dendronized NBIs with m = 1 and 2. The transition temperatures and enthalpies also increased dramatically in the NBI derivatives compared to the PBI derivatives, presumably due to much stronger intermolecular interactions between fluorinated dendrons.

DOI: 10.1021/ja510643b
J. Am. Chem. Soc. 2015, 137, 807−819

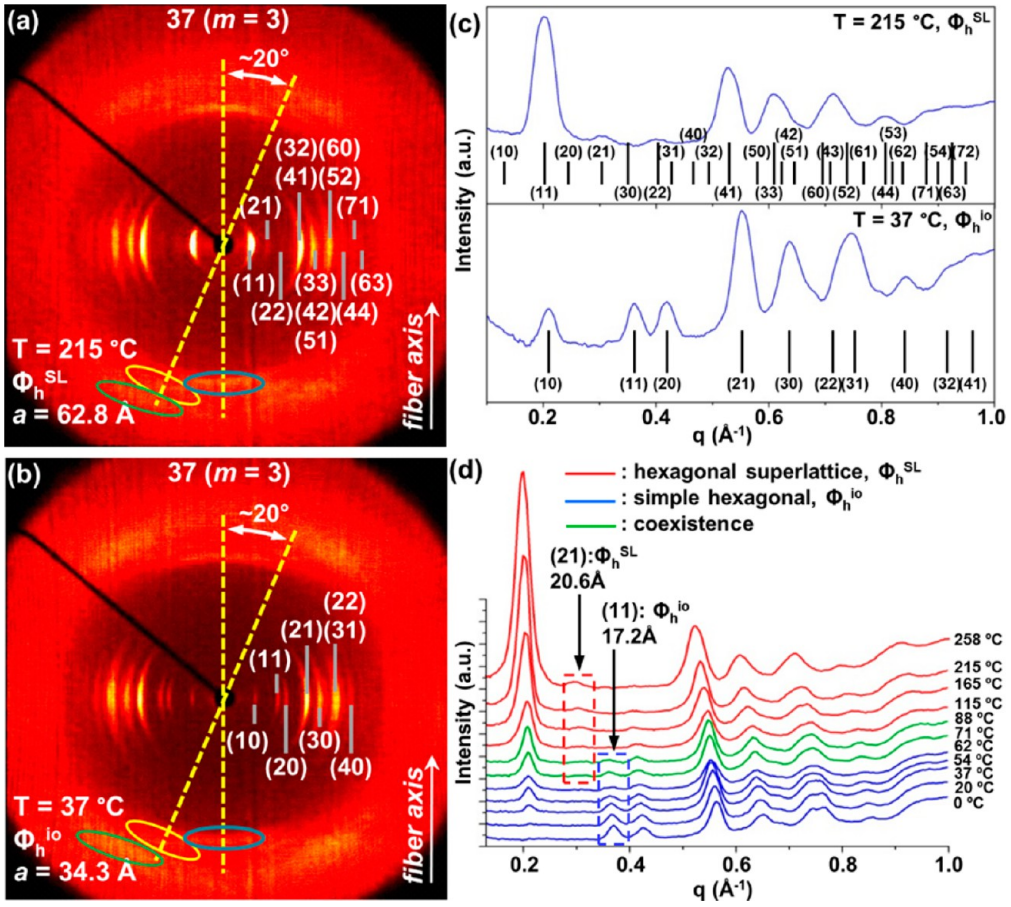

Figure 3. XRD patterns of **37** (m = 3) collected from an oriented fiber in (a) a 2D hexagonal superlattice (Φ_h^{SL}) at 215 °C and (b) a 2D hexagonal phase with intracolumnar order (Φ_h^{io}) at 37 °C. Colored ellipses indicate meridional (blue) and off-meridional (yellow and green) features. (c) 1D meridional plots of fiber XRD patterns for the two phases. The expected positions of reflections and their indices are marked. In the top panel, long lines are used for reflections that are observed in both phases, whereas short lines are used for reflections that are observed only in the superlattice. (d) Temperature-dependent 1D powder XRD plots collected during cooling at a rate of 10 °C/min. Blue XRD plots indicate Φ_h^{io}, red XRD plots indicate Φ_h^{SL}, and green XRD plots indicate coexistence of Φ_h^{io} and Φ_h^{SL}.

Table 2. Structural Analysis of 34, 35 (m = 1), 36 (m = 2), and 37 (m = 3) by XRD

compound	T (°C)	phase[a]	spacing[b] (Å), D_{col}[c] (Å)	ρ[d] (g/cm^3)	M_w[e]	d_{100}, d_{200}, d_{300}, d_{400}, d_{500} (Å)[g]; d_{100}, d_{110}, d_{200}, d_{210}, d_{220}, d_{300}, d_{320}, d_{400}, d_{500}, d_{520} (Å)[h]; d_{10}, d_{11}, d_{20}, d_{21}, d_{30}, d_{22}, d_{31}, d_{40} (Å)[i]; d_{11}, d_{21}, d_{22}, d_{32}, d_{41}, d_{33}, d_{42}, d_{51}, d_{60}, d_{52}, d_{44}, d_{71}, d_{63} (Å)[j]
34	25	**Lam**[k]	d = 25.3	1.57	1191	25.3, 12.7, 8.4, 6.3, –[g]
35	250	**Lam**[k]	d = 31.0	1.67	2415	31.0, 15.6, 10.3, –, 6.2[g]
36	200	**Lam**[k]	d = 22.6	1.66	2443	22.6, 11.3, 7.5, –, –[g]
37	20	Φ_{tetra}^{k}[f]	a = 31.1	1.64	2471	31.1, 22.0, 15.6, 13.9, 11.0, 10.4, 8.6, 7.8, 6.2, 5.8[h]
	37	Φ_h^{io}	a = 34.3 D_{col} = 34.3	1.64	2471	29.7, 17.2, 14.9, 11.2, 9.9, 8.6, 8.2, 7.4[i]
	215	Φ_h^{SL}	a = 62.8 D_{col} = 36.3	1.64	2471	31.4, 20.6, 15.7, 12.5, 11.9, 10.5, 10.3, 9.8, 9.1, 8.7, 7.9, 7.2, 6.9[j]

[a]Phase notation: **Lam**[k], lamellar crystalline phase; Φ_{tetra}^{k}, columnar tetragonal crystalline phase; Φ_h^{io}, 2D simple hexagonal phase with intracolumnar order; Φ_h^{SL}, 2D hexagonal superlattice; [b]Lattice parameters determined from fiber and powder XRD experiments. [c]Column diameter calculated using $D_{col} = a$ for Φ_h^{io}, and $D_{col} = a/3^{1/2}$ for Φ_h^{SL}. [d]Experimental density measured at 20 °C. [e]Molecular weight of the compound. [f]Phase observed only in the as prepared sample. [g]Experimental diffraction peak d-spacing for the **Lam**[k] phase. [h]Experimental diffraction peak d-spacing for the Φ_{tetra}^{k} phase. [i]Experimental diffraction peak d-spacing for the Φ_h^{io} phase. [j]Experimental diffraction peak d-spacing for the Φ_h^{SL} phase.

From DSC analysis, compound **37** appears to exhibit only a single thermodynamically controlled phase after the first heating scan. A tetragonal crystalline phase, Φ_{tetra}^{k}, was observed only in the as prepared sample (by precipitation from solution) during first heating with a melting temperature of 142 °C (Figure 2). This phase could not be reformed during subsequent heat treatments even with a cooling and heating rate of 1 °C/min (Figure SF1). Therefore, the increase of the spacer length from m = 2 to 3 eliminated the crystallization of **37** into a lamellar crystal. Interestingly, the isotropization temperature (297 °C) of **37** is even higher than that of **36** with m = 2 and is similar to that of **35** with m = 1, suggesting that the molecular arrangement of **37** in its supramolecular assembly may be different from **35** and **36**. Indeed, a detailed

DOI: 10.1021/ja510643b
J. Am. Chem. Soc. 2015, 137, 807–819

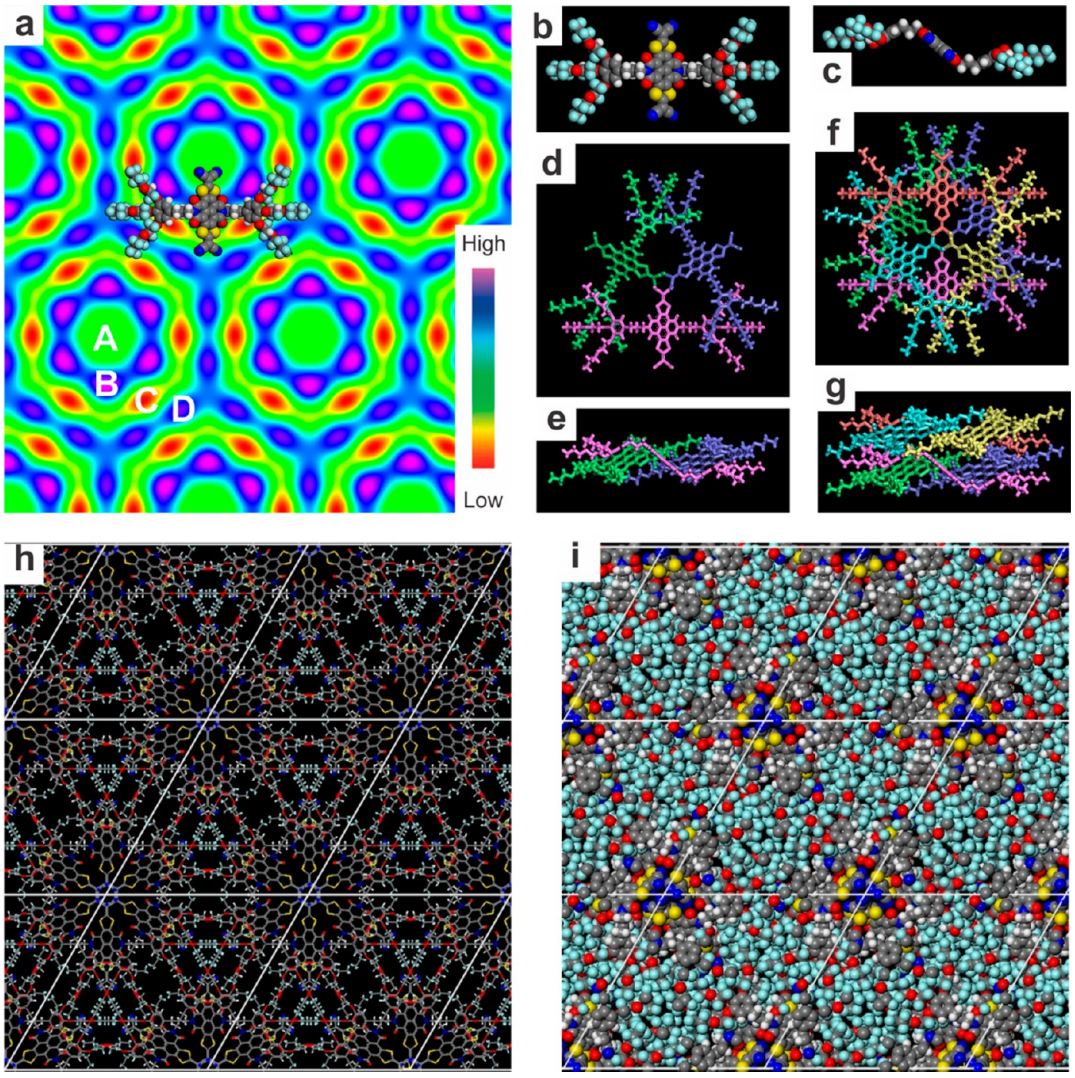

Figure 4. Low-temperature simple 2D Φ_h^{io} phase of **37** (m = 3). (a) Reconstructed electron density map overlaid with one molecule. A, B, C, and D denote regions of electron density and are discussed in the text. (b) CPK model of the molecule, top view and (c) side view. Atoms are colored by element: C, gray; N, blue; S, yellow; H, white; F, light blue. Stick model of a trimer with molecules colored differently, (d) top view and (e) side view. Stick model of a hexamer, (f) top view and (g) side view. (h) Supramolecular columns as constructed in the hexagonal lattice. Atoms colored as in (b). (i) A snapshot of the molecular model in lattice during molecular dynamics simulation. Atoms colored as in (b).

temperature-dependent XRD analysis of compound **37** revealed a 2D columnar hexagonal periodic array with intracolumnar order (Φ_h^{io}) at low temperature and a complex hexagonal superlattice (Φ_h^{SL}), also 2D with intracolumnar order, at high temperature. XRD temperature scans demonstrate that the transition between these two phases is reversible and shows little dependence on rate. Therefore, both hexagonal periodic arrays are thermodynamically controlled.

However, no first-order phase transition between the two phases of **37** is evident by DSC. Therefore, this phase transition can be observed only by XRD experiments performed at different temperatures. The phase transition temperatures, phases, and the associated enthalpy changes obtained for the four compounds with scan rates of 10 °C/min and 1 °C/min are summarized in Table 1.

Structural Analysis of 37 (m = 3) Based on XRD Fiber Patterns and Reconstructed Electron Density Maps. The 3D lamellar assemblies of **34**, **35** (m = 1), and **36** (m = 2) are discussed in the Supporting Information. The XRD fiber patterns collected from the oriented fiber of **37** (m = 3) during first cooling (Figure 3a,b) reveal a 2D hexagonal arrangement of the supramolecular columns. The columns of this periodic array exhibit intracolumnar order. Sharp equatorial reflections indicate well-ordered molecular packing within the *ab*-plane. At low temperatures, the lattice parameter of Φ_h^{io} is a = 34.3 Å. The meridional reflections indicate an interlayer stacking distance of 7.0 Å, which corresponds to the distance between repeat units along the column axis. Combining the lattice dimensions and the experimental density (1.64 g/cm^3, Table 2) measured at 20 °C, each layer within the lattice contains three molecules, which suggests the column stratum is constructed of trimers (Figure 4d), spaced 7.0 Å apart. While most of the observed diffraction peaks change little at high temperature, the (10) reflection of Φ_h^{io} becomes much stronger, the (11) reflection of Φ_h^{io} disappears, and an extra reflection in between the (10) and (11) peaks appears (Figure 3d). The diffraction pattern at high temperature is best fitted with another hexagonal lattice of larger dimensions than that at low temperature, in which the original (10) peak of Φ_h^{io} is assigned to (11), and the emergent reflection is assigned to

DOI: 10.1021/ja510643b
J. Am. Chem. Soc. 2015, 137, 807−819

(21) (Figure 3c). This indicates a phase transition from Φ_h^{io} to a three column hexagonal superlattice (Φ_h^{SL}) with a lattice parameter a = 62.8 Å at 215 °C. The transition from Φ_h^{io} to Φ_h^{SL} is not observed as a first-order transition in the DSC experiments of **37** (Figure 2). However, this transition is detected very clearly between 70 and 90 °C by XRD experiments as shown by the green XRD plots in Figure 3d. The intensities of diffraction peaks that belong solely to the Φ_h^{SL} superlattice are weak. Indeed, only a few of them have been experimentally observed: (21), (32), (42), and (51). This suggests that the Φ_h^{SL} superlattice has a very similar structure to that of the Φ_h^{io} phase, with only slight distortion or modulation.

The wide-angle region of the fiber patterns collected in the Φ_h^{SL} and Φ_h^{io} phases of **37** (Figure 3a,b, respectively) exhibits similar features: a sharp meridional feature at ∼7 Å, indicative of an intracolumnar correlation length of at least 100 Å and two pairs of off-meridional features (yellow and green ellipses). The first pair of off-meridional features (yellow ellipses) are observed at the same q_z (meridional or 00L component of q) as the sharp 7 Å meridional feature, suggesting a tilt conformation with respect to the column axis. The 20° tilt indicated in Figure 3a,b is in good accordance with the molecular model presented in Figure 4. Both wider-angle off-meridional features are significantly broader than the meridional 7 Å feature, suggesting weak column-to-column correlations.

Figure 3c shows 1D meridional plots obtained from fiber XRD patterns plots of the two phases and the indexing of their reflections. Reflections expected only in the Φ_h^{SL} phase are marked with short lines, while reflections observed in both phases are marked with long lines. It can be observed that the diffraction intensities of those peaks observed only in the Φ_h^{SL} phase are weak, and only (21), (42), and (43) have intensities that significantly contribute to changes in electron density distribution between the three columns in the superlattice unit cell. This suggests that the high-temperature Φ_h^{SL} phase is a small modification of the low-temperature Φ_h^{io} phase. From the temperature-dependent 1D powder XRD plots (Figure 3d), a continuous change of intensity can be identified for the reflection at lowest q ((10) reflection for Φ_h^{io} (blue region in Figure 3d) and (11) reflection for Φ_h^{SL} (red region in Figure 3d)) which suggests that the relative electron density between the NBI core region and the dendron column region changes continuously with temperature. The temperature-dependent molecular tilt and change in the arrangement of the NBI derivative within the supramolecular column are responsible for the change in relative electron density between different regions of the lattice.

At room temperature, the Φ_h^{io} phase consists of columns with a diameter of 34.3 Å. The reconstructed electron density map of the low-temperature Φ_h^{io} phase, generated from the fiber XRD pattern in Figure 3b, is shown in Figure 4a. Phase assignments (Tables ST1 and ST2) were based on the physical merit of the electron density maps (Figures SF4 and SF5); that is, showing good separation of regions of different electron densities and being reconcilable to a physical model consistent with the dimensions and shape of the molecules. A detailed discussion of the reconstruction and selection of electron density maps is provided in Section 7 of the Supporting Information, and other choices of maps are shown in Figures SF4 and SF5. The map from Figure 4a can be interpreted as a hexagonal packing of supramolecular columns. In the fiber XRD pattern the first layer line is observed at q_z = 0.90 Å^{-1} (corresponding to a d-spacing of 7.0 Å). Taking this to be the thickness between the column strata, and considering the molar mass (2471 g/mol) and density (1.64 g/cm^3) of the compound, the number of molecules per column stratum in the columns can be calculated to be 2.97, or close to 3. A molecular model of the supramolecular column can therefore be constructed. In each molecule, the dendrons at the two ends adopt a "trans"-like conformation when attached to the rigid core (Figure 4b,c). In each 7.0 Å layer, three molecules form a triangular arrangement (trimer), with their cyano groups gathering in the center (Figure 4d,e). For better packing of space, the trimer is flipped and rotated by 180° in the next layer of 7 Å above and thus forms a hexamer (Figure 4f,g). The column is then simply a stack of hexamers. The molecular columns in the hexagonal lattice as constructed (Figure 4h) and during molecular dynamics simulation (Figure 4i) are shown in comparison with the reconstructed electron density map of the Φ_h^{io} phase (Figure 4a). Four distinct regions (A, B, C, and D) can be identified in the reconstructed electron density map. Region A at the center of the column has medium electron density corresponding to the cyano groups which are not particularly well packed. The high electron density region B corresponds to the aromatic NBI core. The lowest electron density region C corresponds to the aliphatic spacer and the aromatic portion of the attached dendron and is also the region least accessible to other parts of the molecule. Another high electron density region D is found at the boundary between columns where semifluorinated chains can pack efficiently.

The lattice parameter, a, for Φ_h^{SL} is 62.8 Å, which is ∼$3^{1/2}$ times larger than that of the low-temperature Φ_h^{io} phase (a = 34.3 Å) (Table 2). This indicates that in each unit cell of the Φ_h^{SL} phase there are three columns instead of one. The reconstructed electron density map of the Φ_h^{SL} superlattice (Figures 5a and SF5) clearly shows the presence of two

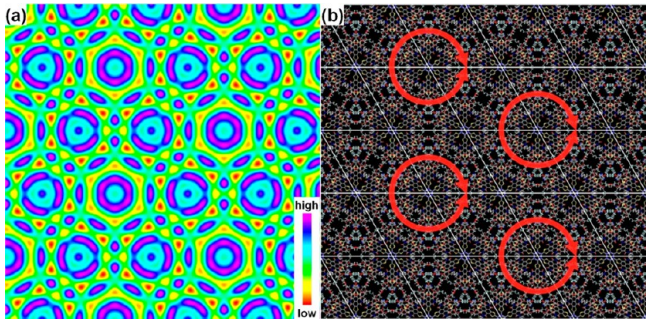

Figure 5. High-temperature hexagonal superlattice Φ_h^{SL} of **37** (m = 3). (a) Reconstructed electron density map. (b) Initial model for the structure of the columns of the hexagonal superlattice.

different types of column, the first type with proper six-fold symmetry comprising one-third of all columns in the superlattice and the second type with only three-fold symmetry comprising the remaining two-thirds of all columns. Nevertheless, the structures of the Φ_h^{io} and Φ_h^{SL} phases must be similar, attested by the similarity of the reconstructed electron density map of the Φ_h^{SL} phase (Figure 5a) to that of the Φ_h^{io} phase (Figure 4a) and also by the similar features observed in the wide-angle region of the fiber XRD patterns of the Φ_h^{SL} phase and Φ_h^{io} phase (Figure 5a,b, respectively). Note that, since the electron density map in Figure 5a and the

DOI: 10.1021/ja510643b
J. Am. Chem. Soc. 2015, 137, 807−819

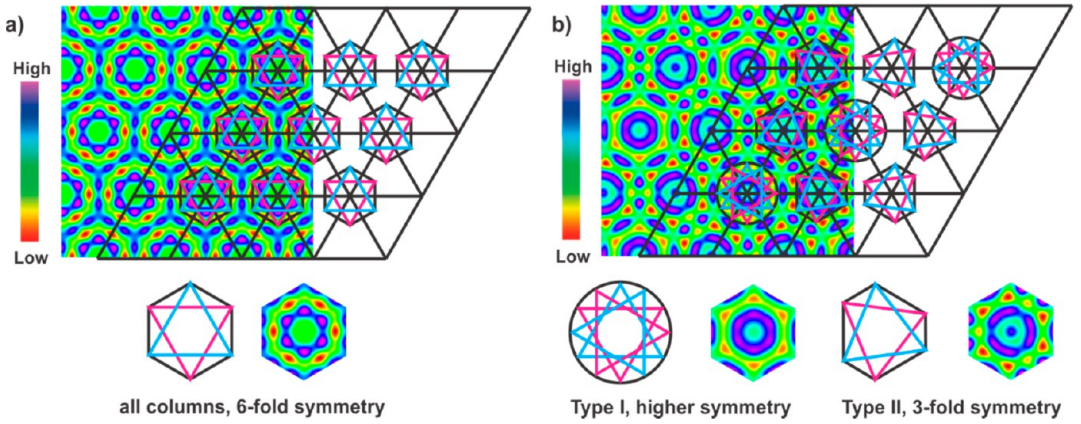

Figure 6. Revised model for Φ_h^{io} and Φ_h^{SL} of **37** (m = 3). Reconstructed electron density map overlaid with schematic representation of column structure for (a) the low-temperature Φ_h^{io} phase and (b) the high-temperature Φ_h^{SL}.

corresponding physical structure were calculated using the measured XRD data, they are by construction consistent with both the missing and absent peaks in the superlattice diffraction pattern.

Our initial model for the structure of the columns of the Φ_h^{SL} phase (Figure 5b) was consistent with the XRD and reconstructed electron density data and accounts for the presence of two distinct types of column in the superlattice. The rationale behind the model was that, at high temperatures, the semifluorinated end groups at the periphery of the columns would prefer coordinated movement (vibration or rotation, clockwise, or counterclockwise). This would require the neighboring columns to vibrate or rotate in the opposite direction. Such coordinated movement cannot be satisfied by all columns in a hexagonal lattice as each column neighbors three others. This problem is solved by having one in three columns exhibit fully coordinated vibration or rotation (hence six-fold symmetry), while the other two only partially possess that freedom (three-fold symmetry). However, solid-state NMR studies to be discussed later do not indicate special mobility of the semifluorinated parts of the dendron, even at elevated temperatures, contradicting this initial model.

A revised structural model for Φ_h^{SL} was designed that is consistent not only with the XRD and reconstructed electron density data but also with data derived from solid-state NMR experiments. Reconstructed electron density maps and schematics of the low-temperature Φ_h^{io} phase and high-temperature Φ_h^{SL} superlattice are shown in Figure 6a,b, respectively. The structure of the Φ_h^{io} phase is as described earlier, whereby each column is a stack of hexamers (Figure 4f,g). However, the structure of the Φ_h^{SL} superlattice contains two types of columns, each different to those proposed in the initial model. One-third of columns (Type I) consist of a helix of higher rotational symmetry formed from the stacking of dendronized NBI hexamers, whereas two-thirds of columns (Type II) consist of a three-fold symmetric column of distorted hexamers. In each hexamer in a Type II column, the two constituent trimers are rotated such that the resultant hexamer has only three-fold symmetry, unlike the higher symmetry exhibited in the low-temperature Φ_h^{io} phase. Geometric considerations necessitate the presence of lower-symmetry columns, to maximize the efficiency of space packing between columns and to avoid clashes between columns, as would occur with completely round columns. This revised model, unlike our initial model, does not require rapid movement of the semifluorinated end groups and is supported by solid-state NMR experiments as well as XRD data, although this phase transition between the Φ_h^{io} and Φ_h^{SL} phases is not detectable by DSC.

Solid-State NMR Studies of 37 (m = 3). The two models for the structure of the Φ_h^{SL} phase, both of which are consistent with XRD experimental data, can be distinguished by a combination of ^{1}H, ^{13}C and ^{19}F solid-state NMR, which probe both the structure *and* the dynamics of individual chemical groups.[41−43] These experiments exploit the sensitivity of ^{1}H and ^{19}F NMR chemical shifts and line widths to local packing and dynamics, respectively; the sensitivity of chemical shifts to local conformation in ^{13}C NMR; and ^{1}H−^{13}C correlations indicating spatial proximities in the range of a few Å. In order to determine local motions, dipole−dipole couplings between the nuclear spins are used to provide an internal clock of a few tens of kHz. Fast motion then means motional rates well above 10 kHz, whereas slow motion means rates well below 1 kHz. Since the dipole−dipole coupling depends on both the *distance* between the coupled spins and the *orientation* of internuclear vectors, rotational motions and fluctuations of individual chemical groups as well as fluctuations between different groups are detected. Furthermore, the amplitudes of the fluctuations of the different moieties can be determined by analysis of the reduced ^{13}C anisotropic chemical shifts.

VT ^{1}H and ^{19}F magic angle spinning (MAS) NMR spectra of **37** were recorded in the temperature range from 10 to 120 °C covering the pure Φ_h^{io} phase from 10 to 62 °C, the pure Φ_h^{SL} phase from 110 to 120 °C, and the coexistence of the two phases from 70 to 90 °C (compare Figures 3d and 7a,b). Both spin species, ^{1}H and ^{19}F, are particularly suitable here due to their high natural abundance and high magnetic moments, which lead to strong dipolar interactions on the order of tens of kHz and to broad NMR lines in the absence of motion. Molecular reorientations in the 10−100 kHz range average these local anisotropic NMR interactions, leading to a significant line narrowing in MAS NMR spectra. In the ^{19}F NMR spectra of **37** (m = 3) (Figure 7), such line narrowing is observed in the low-temperature Φ_h^{io} phase, in the range 0−40 °C (indicated by the blue rectangle in Figure 7). It should be noted that this line narrowing happens for all ^{19}F sites in the same temperature range, excluding motional processes triggered from the chain ends of the semifluorinated parts of the dendrons. At temperatures above 40 °C only a minor

DOI: 10.1021/ja510643b
J. Am. Chem. Soc. 2015, 137, 807−819

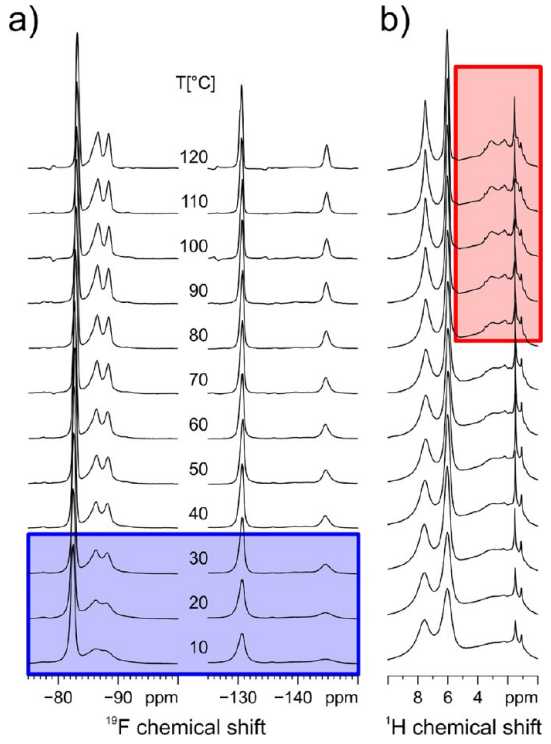

Figure 7. (a) VT ^{19}F MAS NMR and (b) ^{1}H MAS NMR spectra recorded at 25 kHz MAS spinning frequency and 500.13 MHz ^{1}H Larmor frequency. The blue and red rectangles indicate the temperature ranges over which changes in the dynamic behavior of **37** were monitored by ^{19}F or ^{1}H MAS NMR line width, respectively.

gradual homogeneous line narrowing is observed at all ^{19}F sites of **37**. Even at the highest temperature achievable with the experimental setup (120 °C), the sample exhibits well resolved but relatively broad ^{19}F NMR signals indicating rapid but highly restricted molecular reorientations.[41]

It is interesting to compare these findings with a similar NMR study of semifluorinated alkanes.[44] There the ^{19}F and ^{13}C MAS NMR spectra exhibited significant changes in chemical shifts in response to conformational changes and molecular reorganization. In contrast, the temperature-dependent ^{19}F MAS NMR spectra of **37** do not show any chemical shift changes over the entire temperature range surveyed. Therefore, significant changes in local density or local chain conformations of the semifluorinated groups can be eliminated as the origin of superlattice formation. Nevertheless, the local fluctuation of the semifluorinated groups may facilitate the transition to the superlattice, as these fluctuations are already present more than 30 °C below the onset of the transition.

In contrast, motional narrowing of the ^{1}H NMR signals of the aliphatic linker between dendron and NBI core is only observed in the Φ_h^{SL} phase at temperatures above 90 °C, as indicated by the red rectangle in Figure 7. The coincidence of the thermal activation of rapid molecular reorientation in the m = 3 aliphatic linker and the formation of the Φ_h^{SL} phase suggests that a complex reorientation of the propylene linker is involved in the transition from the Φ_h^{io} phase to the Φ_h^{SL} superlattice.

Taken together, the ^{1}H and ^{19}F NMR spectra in Figure 7 allow discrimination between the two proposed structures for the Φ_h^{SL} phase. Unlike first-order phase transitions, for which the time scale of dynamics typically changes by orders of magnitude (for example at a solid−liquid phase transition), higher order phase transitions, such as that from Φ_h^{io} to Φ_h^{SL}, may occur with a more gradual change in motional rate. Thus, any additional mobility present in Φ_h^{SL} at higher temperature may be very slow at the transition temperature itself and may increase continuously with temperature. The line narrowing observed by ^{1}H NMR (Figure 7b) clearly demonstrates a continuous increase in mobility of the propylene linker above the temperature at which Φ_h^{SL} is formed. However, no concomitant increase in mobility is observed by ^{19}F NMR in the semifluorinated chains (Figure 7a). Thus, the requirement of our initial model (Figure 5) that the semifluorinated chains undergo coordinated motion is unfulfilled, and hence our initial model can be discounted. Our revised model (Figure 6), however, which does not require such coordinated motion, is supported by the data from VT NMR.

In order to gain further insight into the different packing in the Φ_h^{io} and Φ_h^{SL} phases, 2D ^{13}C{^{1}H} heteronuclear Lee−Goldburg cross-polarization (LGCP) correlation experiments were performed (Figure 8).[45] Such ^{13}C{^{1}H} heteronuclear correlation experiments are commonly used to clarify the spectral assignment for the NMR spectra in the solid state and to probe spatial proximities between ^{1}H and ^{13}C sites in the local molecular packing arrangement. Comparison of the 2D correlation spectrum of the Φ_h^{io} phase at 40 °C with that of the

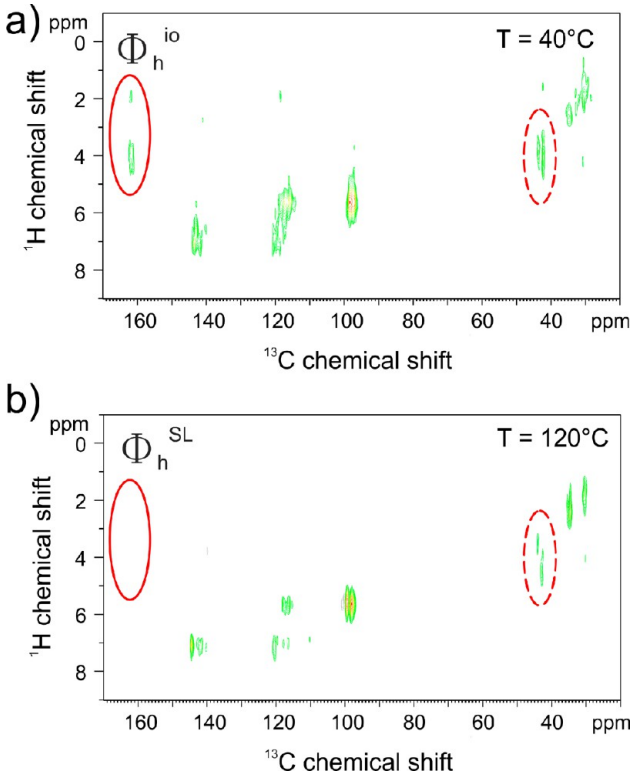

Figure 8. ^{13}C{^{1}H} heteronuclear LGCP correlation spectra of **37** (m = 3) recorded at 18 kHz MAS and 700.23 MHz ^{1}H Larmor frequency using an LGCP contact time of 1 ms and 102 kHz frequency-switched Lee−Goldburg multipulse decoupling for line narrowing in the ^{1}H dimension.[45] The spectrum acquired at 40 °C (a) in the Φ_h^{io} phase shows spatial contacts between the methylene protons of the $(CH_2)_3$ linker and the carbonyl positions of the NBI core (solid red ellipse), which are not observed in the Φ_h^{SL} phase at 120 °C (b). The broken red ellipse indicates the signals of the methylene protons of the $(CH_2)_3$ linker.

DOI: 10.1021/ja510643b
J. Am. Chem. Soc. 2015, 137, 807−819

Φ_h^{SL} superlattice at 120 °C indicates a substantial narrowing of the signals in both dimensions, ^{1}H and ^{13}C. This line narrowing can be attributed to increased molecular fluctuations at elevated temperatures, which average line broadening due to conformational distributions in the ^{13}C dimension and average line broadening due to chemical shift dispersion and dipolar couplings in the ^{1}H dimension, leading in both cases to narrower distributions and thus to better spectral resolution.

Essential to the understanding of the structural differences between the two phases, however, are the differences observed in the signals of the methylene protons in the $(CH_2)_3$ linker adjacent to the NBI core (broken red ellipse, Figure 8). The conformational splitting observed in the ^{13}C dimension of the Φ_h^{io} phase at 40 °C is not averaged to a single signal at 120 °C, as one might expect from the narrowing of the linker signal at 30 ppm. In contrast, the single ^{1}H signal at low temperature splits in the high temperature Φ_h^{SL} superlattice into two different ^{1}H chemical shifts for the two different conformations, indicating two distinct local environments for the chemically equivalent ^{1}H sites. Moreover, it should be noted that the signal intensity of the methylene unit next to the NBI core is significantly reduced compared to the signal intensities of the other methylene units along the linker. Even more pronounced are the differences in the intensity of the carbonyl signals of the NBI core observed at 163 ppm in the ^{13}C dimension (solid red ellipse in Figure 8). In the Φ_h^{io} phase, these carbonyl sites exhibit strong correlations with the sites of the methylene unit next to the NBI core, seen at 4 ppm in the ^{1}H dimension. Even the next nearest CH_2 group, observed slightly below 2 ppm, shows a clear correlation with the carbonyl sites. However, in the Φ_h^{SL} superlattice at 120 °C, no correlation signal for the carbonyl sites is observed. Thus, the heteronuclear dipolar coupling needed to generate the correlation signals has been reduced by molecular motion, which changes the distance between, and relative orientation of, the correlating sites. Since all ^{1}H−^{13}C correlations in the semifluorinated dendron are observed in both the low- and the high-temperature phases, the fading of the carbonyl correlation signals indicates a fast reorientation of the linking methylene units relative to the NBI core. Unfortunately, the carbonyl signals are the only signals in the correlation spectrum that can be unambiguously assigned to the NBI core. Therefore, the correlation spectra cannot provide further information on the dynamic modes of the NBI core.

Since molecular reorientations average not only heteronuclear dipolar couplings but also chemical shift anisotropy, the acquisition of ^{13}C chemical shift anisotropy (CSA) sideband patterns under slow MAS conditions provides an additional approach to monitor molecular reorientations. Due to their substantial CSA, aromatic and carbonyl sites are particularly well suited for these studies.[41,46] Figure 9 shows the ^{13}C CP-MAS sideband pattern recorded at 5 kHz MAS and 700.23 MHz ^{1}H Larmor frequency in the low- and high-temperature phases of **37**. The sideband pattern of the carbonyl sites is indicated by the red lines. Remarkably, despite the significant difference in intensity, only minor differences are observed in the patterns of the Φ_h^{io} phase and Φ_h^{SL}. Pronounced large angle fluctuations typically cause substantial differences in the orientation and magnitude of the chemical shift anisotropy, and therefore the presence of large angle fluctuations of the NBI core in the high-temperature phase can be safely excluded.

Solid-state NMR experiments proved vital in distinguishing between the two structural models proposed for the Φ_h^{SL} phase of **37**, both of which were consistent with XRD data. Whereas

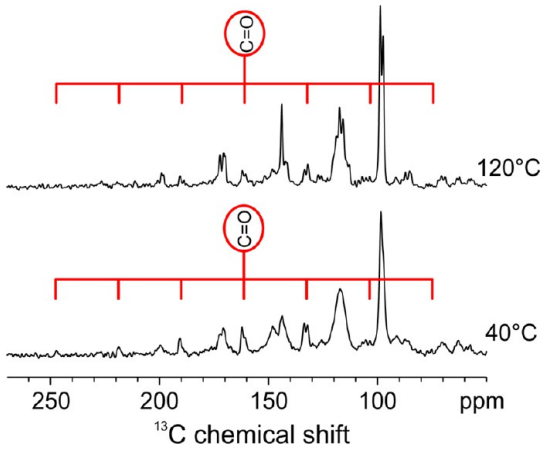

Figure 9. ^{13}C CP-MAS spectra of **37** (m = 3) recorded at 5 kHz MAS and 700.23 MHz ^{1}H Larmor frequency using a CP contact time of 2 ms. The MAS sideband pattern (indicated with red lines) of the Φ_h^{io} phase at 40 °C and that of the Φ_h^{SL} superlattice at 120 °C show only minor differences.

XRD is a powerful structural probe, solid-state NMR can provide information on both the structure *and* the dynamics of the individual groups of the molecular building blocks in the two supramolecular structures. No changes in the structure for both the fluorinated side groups and the $(CH_2)_3$ linker are visible in 1D NMR spectra. However, rotational motions leading to line narrowing are clearly observed. In order for line narrowing to occur, these motions must be in the range of kHz or faster. In the fluorinated side groups such motions occur in the low-temperature Φ_h^{io} phase already, whereas for the flexible linker they occur only in the Φ_h^{SL} phase. The line narrowing increases continuously with temperature, in accord with the fact that no first-order phase transition was observed. Remarkably, no motional gradient over the entire semifluorinated groups is observed, excluding rearrangements triggered by the chain ends of the dendron. The motions for the semifluorinated groups, the $(CH_2)_3$ linkers and the NBI core are highly restricted and involve angular fluctuations below ±25°.

Therefore, of the two structures originally derived from XRD data (Figures 5 and 6b), only the second one is in accord with these findings. Thus, our multitechnique approach combining XRD and solid-state NMR allows us to specify the structure and dynamics of this complex supramolecular system. This information is not available from either of these two techniques alone. Such multitechnique approaches will become increasingly important in the future. Indeed, they have recently been able to elucidate the packing in a semiconducting polymer for organic electronics.[47]

■ CONCLUSIONS

The synthesis and structural analysis of strongly electron-accepting NBI functionalized with an environmentally friendly chiral racemic semifluorinated alkyl group and with an AB_3 minidendron containing the same semifluorinated group are reported. The NBI with the semifluorinated group and the NBIs with the dendron attached via one and two methylenic units (m = 1, 2) to the imide groups of the NBI core self-organize in lamellar crystals. The lamellar crystals obtained from m = 1 are generated via a thermodynamically controlled process, while the other two via a kinetically controlled process. The dendronized NBI with m = 3 self-assembles into complex

DOI: 10.1021/ja510643b
J. Am. Chem. Soc. 2015, 137, 807−819

columns that self-organize via a thermodynamically controlled process into a Φ_h^{SL} superlattice and a Φ_h^{io} phase with intracolumnar order. The structure of Φ_h^{SL} could be elucidated only by a combination of XRD studies and solid-state NMR experiments. The transition from Φ_h^{io} to Φ_h^{SL} is continuous and therefore does not exhibit a first-order phase transition in the DSC experiments. Previously columnar hexagonal superlattices, Φ_h^{SL}, were obtained only by co-assembly, and no transition from the Φ_h^{SL} to a Φ_h^{io} was observed in a one component system.[48] Therefore, the complex and thermodynamically controlled columnar hexagonal polymorphism reported here is unprecedented, and the simple methods elaborated for the synthesis of its building blocks as well as the method elaborated for its structural analysis will be of great interest for supramolecular organic electronic materials as alternatives to fullerene acceptors in organic photovoltaics[9b−d] and other electronic applications.[8,9,24] Last but not least, the semifluorinated building blocks elaborated here will not be limited to applications in electronic materials and also will find utility in fluorous chemistry as well as in organic, supramolecular, macromolecular, and biomolecular fluorine-containing compounds[35,49] that are neither toxic nor biopersistent.[18,29−32]

■ ASSOCIATED CONTENT

Supporting Information

Experimental procedures with complete spectral and structural analysis. This material is available free of charge via the Internet at http://pubs.acs.org.

■ AUTHOR INFORMATION

Corresponding Author

*percec@sas.upenn.edu

Notes

The authors declare no competing financial interest.

■ ACKNOWLEDGMENTS

Financial support by the National Science Foundation (DMR-1066116, DMR-1120901, and OISE-1243313), the Humboldt Foundation, and the P. Roy Vagelos Chair at Penn (all to V.P.) is gratefully acknowledged. G.U. and X.Z. acknowledge support from the joint NSF-EPSRC PIRE project "RENEW" (EPSRC grant EP-K034308).

■ REFERENCES

(1) Würthner, F. *Chem. Commun.* **2004**, 1564−1579.
(2) Görl, D.; Zhang, X.; Würthner, F. *Angew. Chem., Int. Ed.* **2012**, *51*, 6328−6348.
(3) Huang, C.; Barlow, S.; Marder, S. R. *J. Org. Chem.* **2011**, *76*, 2386−2407.
(4) Suraru, S.-L.; Würthner, F. *Angew. Chem., Int. Ed.* **2014**, *53*, 7428−7448.
(5) Rybtchinski, B.; Sinks, L. E.; Wasielewski, M. R. *J. Am. Chem. Soc.* **2004**, *126*, 12268−12269.
(6) Wasielewski, M. R. *Acc. Chem. Res.* **2009**, *42*, 1910−1921.
(7) Zhang, X.; Rehm, S.; Safont-Sempere, M. M.; Würthner, F. *Nat. Chem.* **2009**, *1*, 623−629.
(8) Facchetti, A. *Chem. Mater.* **2011**, *23*, 733−758.
(9) (a) Anthony, J. E.; Facchetti, A.; Heeney, M.; Marder, S. R.; Zhan, X. *Adv. Mater.* **2010**, *22*, 3876−3892. (b) Schmidt-Mende, L.; Fechtenkötter, A.; Müllen, K.; Moons, E.; Friend, R. H.; MacKenzie, J. D. *Science* **2001**, *293*, 1119−1122. (c) Pho, T. V.; Toma, F. M.; Chabinyc, M. L.; Wudl, F. *Angew. Chem., Int. Ed.* **2013**, *52*, 1446−1451. (d) Hartnett, P. E.; Timalsina, A.; Ramakrishna Matte, H. S. S.; Zhou, N.; Guo, X.; Zhao, W.; Facchetti, A.; Chang, R. P. H.; Hersam, M. C.; Wasielewski, M. R.; Marks, T. J. *J. Am. Chem. Soc.* **2014**, *136*, 16345−16356.
(10) De Greef, T. F. A.; Smulders, M. M. J.; Wolffs, M.; Schenning, A. P. H. J.; Sijbesma, R. P.; Meijer, E. W. *Chem. Rev.* **2009**, *109*, 5687−5754.
(11) Heek, T.; Würthner, F.; Haag, R. *Chem.—Eur. J.* **2013**, *19*, 10911−10921.
(12) Krieg, E.; Weissman, H.; Shimoni, E.; Bar On Ustinov, A.; Rybtchinski, B. *J. Am. Chem. Soc.* **2014**, *136*, 9443−9452.
(13) Gsänger, M.; Oh, J. H.; Könemann, M.; Höffken, H. W.; Krause, A.-M.; Bao, Z.; Würthner, F. *Angew. Chem., Int. Ed.* **2010**, *49*, 740−743.
(14) Percec, V.; Sun, H.-J.; Leowanawat, P.; Peterca, M.; Graf, R.; Spiess, H. W.; Zeng, X.; Ungar, G.; Heiney, P. A. *J. Am. Chem. Soc.* **2013**, *135*, 4129−4148.
(15) Percec, V.; Peterca, M.; Tadjiev, T.; Zeng, X.; Ungar, G.; Leowanawat, P.; Aqad, E.; Imam, M. R.; Rosen, B. M.; Akbey, U.; Graf, R.; Sekharan, S.; Sebastiani, D.; Spiess, H. W.; Heiney, P. A.; Hudson, S. D. *J. Am. Chem. Soc.* **2011**, *133*, 12197−12219.
(16) Percec, V.; Hudson, S. D.; Peterca, M.; Leowanawat, P.; Aqad, E.; Graf, R.; Spiess, H. W.; Zeng, X.; Ungar, G.; Heiney, P. A. *J. Am. Chem. Soc.* **2011**, *133*, 18479−18494.
(17) Yamashita, Y.; Suzuki, T.; Saito, G.; Mukai, T. *J. Chem. Soc., Chem. Commun.* **1986**, 1489−1491.
(18) Wilson, C. J.; Wilson, D. A.; Feiring, A. E.; Percec, V. *J. Polym. Sci., Part A: Polym. Chem.* **2010**, *48*, 2498−2508.
(19) Percec, V.; Imam, M. R.; Bera, T. K.; Balagurusamy, V. S. K.; Peterca, M.; Heiney, P. A. *Angew. Chem., Int. Ed.* **2005**, *44*, 4739−4745.
(20) Percec, V.; Johansson, G.; Ungar, G.; Zhou, J. *J. Am. Chem. Soc.* **1996**, *118*, 9855−9866.
(21) Johansson, G.; Percec, V.; Ungar, G.; Zhou, J. P. *Macromolecules* **1996**, *29*, 646−660.
(22) Percec, V.; Schlueter, D.; Kwon, Y. K.; Blackwell, J.; Moeller, M.; Slangen, P. J. *Macromolecules* **1995**, *28*, 8807−8818.
(23) Percec, V.; Glodde, M.; Peterca, M.; Rapp, A.; Schnell, I.; Spiess, H. W.; Bera, T. K.; Miura, Y.; Balagurusamy, V. S. K.; Aqad, E.; Heiney, P. A. *Chem.—Eur. J.* **2006**, *12*, 6298−6314.
(24) Percec, V.; Glodde, M.; Bera, T. K.; Miura, Y.; Shiyanovskaya, I.; Singer, K. D.; Balagurusamy, V. S. K.; Heiney, P. A.; Schnell, I.; Rapp, A.; Spiess, H.-W.; Hudson, S. D.; Duan, H. *Nature* **2002**, *419*, 384−387.
(25) Hudson, S. D.; Jung, H. T.; Percec, V.; Cho, W.-D.; Johansson, G.; Ungar, G.; Balagurusamy, V. S. K. *Science* **1997**, *278*, 449−452.
(26) Percec, V.; Aqad, E.; Peterca, M.; Imam, M. R.; Glodde, M.; Bera, T. K.; Miura, Y.; Balagurusamy, V. S. K.; Ewbank, P. C.; Würthner, F.; Heiney, P. A. *Chem.—Eur. J.* **2007**, *13*, 3330−3345.
(27) Dukeson, D. R.; Ungar, G.; Balagurusamy, V. S. K.; Percec, V.; Johansson, G. A.; Glodde, M. *J. Am. Chem. Soc.* **2003**, *125*, 15974−15980.
(28) Percec, V.; Imam, M. R.; Peterca, M.; Leowanawat, P. *J. Am. Chem. Soc.* **2012**, *134*, 4408−4420.
(29) Zhang, W. *Green Chem.* **2009**, *11*, 911−920.
(30) Guo, J.; Resnick, P.; Efimenko, K.; Genzer, J.; DeSimone, J. M. *Ind. Eng. Chem. Res.* **2007**, *47*, 502−508.
(31) Renner, R. *Environ. Sci. Technol.* **2006**, *40*, 2866−2867.
(32) Renner, R. *Environ. Sci. Technol.* **2001**, *35*, 154A−160A.
(33) Bertin, A.; Steibel, J.; Michou-Gallani, A.-I.; Gallani, J.-L.; Felder-Flesch, D. *Bioconjugate Chem.* **2009**, *20*, 760−767.
(34) Fiuza, S. M.; Gomes, C.; Teixeira, L. J.; Girão da Cruz, M. T.; Cordeiro, M. N. D. S.; Milhazes, N.; Borges, F.; Marques, M. P. M. *Bioorg. Med. Chem.* **2004**, *12*, 3581−3589.
(35) Rosen, B. M.; Wilson, C. J.; Wilson, D. A.; Peterca, M.; Imam, M. R.; Percec, V. *Chem. Rev.* **2009**, *109*, 6275−6540.
(36) Percec, V.; Glodde, M.; Johansson, G.; Balagurusamy, V. S. K.; Heiney, P. A. *Angew. Chem., Int. Ed.* **2003**, *42*, 4338−4342.
(37) Röger, C.; Würthner, F. *J. Org. Chem.* **2007**, *72*, 8070−8075.
(38) Hatchard, W. R. *J. Org. Chem.* **1964**, *29*, 660−665.

DOI: 10.1021/ja510643b
J. Am. Chem. Soc. 2015, 137, 807−819

(39) Gao, X.; Di, C.; Hu, Y.; Yang, X.; Fan, H.; Zhang, F.; Liu, Y.; Li, H.; Zhu, D. *J. Am. Chem. Soc.* **2010**, *132*, 3697−3699.
(40) Percec, V.; Dulcey, A. E.; Balagurusamy, V. S. K.; Miura, Y.; Smidrkal, J.; Peterca, M.; Nummelin, S.; Edlund, U.; Hudson, S. D.; Heiney, P. A.; Duan, H.; Magonov, S. N.; Vinogradov, S. A. *Nature* **2004**, *430*, 764−768.
(41) Hansen, M. R.; Graf, R.; Spiess, H. W. *Acc. Chem. Res.* **2013**, *46*, 1996−2007.
(42) Tonelli, A. E.; Schilling, F. C. *Acc. Chem. Res.* **1981**, *14*, 233−238.
(43) Schmidt-Rohr, K.; Spiess, H. W. *Multidimensional Solid-State NMR and Polymers*; Academic Press: New York, 1994.
(44) Lee, Y. J.; Clark, C. G.; Graf, R.; Wagner, M.; Müllen, K.; Spiess, H. W. *J. Phys. Chem. B* **2009**, *113*, 1360−1366.
(45) van Rossum, B.-J.; Foerster, H.; deGroot, H. J. M. *J. Magn. Reson.* **1997**, *124*, 516−519.
(46) Hansen, M. R.; Schnitzler, T.; Pisula, W.; Graf, R.; Müllen, K.; Spiess, H. W. *Angew. Chem., Int. Ed.* **2009**, *48*, 4621−4624.
(47) Dudenko, D.; Kiersnowski, J.; Shu, W.; Pisula, W.; Sebastiani, D.; Spiess, H. W.; Hansen, M. R. *Angew. Chem., Int. Ed.* **2012**, *51*, 11068−11072.
(48) (a) Percec, V.; Ahn, C. H.; Bera, T. K.; Ungar, G.; Yeardley, D. J. P. *Chem.—Eur. J.* **1999**, *5*, 1070−1083. (b) Percec, V.; Bera, T. K.; Glodde, M.; Fu, Q. Y.; Balagurusamy, V. S. K.; Heiney, P. A. *Chem.—Eur. J.* **2003**, *9*, 921−935.
(49) (a) Gladysz, J. A.; Curran, D. P.; Horvath, I. T., Eds. *Handbook of Fluorous Chemistry*. Wiley −VCH, Weinheim, Germany, 2004. (b) *Organofluorine Chemistry: Principles and Commercial Applications*; Banks, R. E., Smart, B. E., Tatlow, J. C., Eds.; Plenum Press: New York, 1994. (c) Krafft, M. P.; Riess, J. G. *Chem. Rev.* **2009**, *109*, 1714−1792. (d) Berger, R.; Resnati, G.; Metrangolo, P.; Weber, E.; Hulliger, J. *Chem. Soc. Rev.* **2011**, *40*, 3496−3508. (e) Cametti, M.; Crousse, B.; Metrangolo, P.; Milani, R.; Resnati, G. *Chem. Soc. Rev.* **2012**, *41*, 31−42. (f) Priimagi, A.; Cavallo, G.; Metrangolo, P.; Resnati, G. *Acc. Chem. Res.* **2013**, *46*, 2686−2695.

DOI: 10.1021/ja510643b
J. Am. Chem. Soc. 2015, 137, 807−819